This is the version of the article before peer review or editing, as submitted by an author to NANOTECHNOLOGY.
IOP Publishing Ltd is not responsible for any errors or omissions in this version of the manuscript or any version derived from it.
The Version of Record is available online at https://doi.org/10.1088/1361-6528/aa91c1

A self-ordered, body-centered tetragonal superlattice of SiGe nanodot growth by reduced pressure CVD

Yuji Yamamoto[1,*], Peter Zaumseil[1], Giovanni Capellini[1,2], Markus Andreas Schubert[1], Anne Hesse[1], Marco Albani[3], Roberto Bergamaschini[3], Francesco Montalenti[3], Thomas Schroeder[1,4], and Bernd Tillack[1,5]

[1] IHP, Im Technologiepark, 25, 15236 Frankfurt (Oder), Germany

[2] Dipartimento di Scienze, Università degli Studi Roma Tre, I-00146 Roma, Italy

[3] L-NESS and Dipartimento di Scienza dei Materiali, Università degli Studi di Milano-Bicocca, Via R. Cozzi 55, I-20125 Milano, Italy

[4] BTU Cottbus-Senftenberg, Konrad-Zuse Straße 1, 03046 Cottbus, Germany

[5] Technische Universität Berlin, HFT4, Einsteinufer 25, 10587 Berlin, Germany

*Corresponding author:

Tel: +49 335 56 25 156 Fax: +49 335 56 25 661

E-mail: yamamoto@ihp-microelectronics.com

Abstract

Self-ordered three-dimensional body-centered tetragonal (BCT) SiGe nanodot structures are fabricated by depositing SiGe/Si superlattice layer stacks using reduced pressure chemical vapor deposition. For high enough Ge content in the island (>30%) and deposition temperature of the Si spacer layers (T>700°C), we observe the formation of an ordered array with islands arranged in staggered position in adjacent layers. The in plane periodicity of the islands can be selected by a suitable choice of the annealing temperature before the Si spacer

layer growth and of the SiGe dot volume, while only a weak influence of the Ge concentration is observed. Phase-field simulations are used to clarify the driving force determining the observed BCT ordering, shedding light on the competition between heteroepitaxial strain and surface-energy minimization in the presence of a non-negligible surface roughness.

Keywords

Chemical Vapor Deposition, Epitaxy, SiGe, Nanodot, Self-ordering

PACS

81.15.Gh, 62.23.Eg

1. Introduction

Recent technologies of group IV semiconductor enable the realization of new artificial materials of lower dimensionality, such as superlattice and nanodots structures [1-4], allowing a broadening of the functionalities of optoelectronic devices [5]. In particular, three-dimensional (3D) ordered island crystals could improve the performances of devices such as quantum dot lasers [6, 7]. SiGe or Ge nanodots are promising materials to be integrated into the existing CMOS platform thanks to process and material compatibilities.

The growth of SiGe nanoislands on bare Si surface occurs according to the Stranski-Krastanov dynamics [8], leading to randomly arranged nanoislands. The ordered spatial arrangement of the nanodots on the Si surface can be achieved by growing islands on a pre-patterned substrate [9, 10]. In the case of 3D stacking of Ge nanodots on Si substrates, the Ge nanodots tend to grow vertically aligned, due to the elastic strain field of the buried Ge nanodots, leading to maximum relaxation at on-top positions [11]. Interestingly, vertical ordering in multilayered structures is accompanied by progressive lateral ordering initiated directly on the first dot layer by Si overgrowth [12, 13]. In these references, the vertical alignment of Ge dots was investigated for smooth surface, neglecting any effect related to the Si surface roughness.

In this paper, we present evidence for a self-organized body-centered tetragonal (BCT) SiGe nanodot arrangement of a SiGe nanodot/Si superlattice deposition. Here we choose Ge concentration between 25% to 40%, which results in a lower in strain field and diffusivity compared to that of Ge, and maximum Si growth temperature of 700°C to maintain surface morphology of the deposited Si on the SiGe nanodots. The SiGe nanodot formation mechanism is discussed with support of growth simulations based on a continuum model.

2. Experimental Methods

The SiGe nanodot stacked multi-layers are grown on 200 mm Si (100) wafers using

reduced-pressure (RP) chemical vapor deposition (RPCVD). Standard Radio Corporation of America (RCA) clean followed by HF dip is performed to clean the Si (001) surface and to remove native SiO_2. After loading the Si (001) wafer into the reactor, the wafer is baked at 1000°C in H_2 to remove residual native oxide. After the bake, the wafers are cooled down and a 25 nm to 100 nm thick Si layer is deposited at a temperature in the 675-700°C range using a H_2-SiH_4 gas mixture. After further cooling down to 550°C, a 2.5 nm to 10 nm thick SiGe layer is deposited. The Ge concentration of the SiGe layer is varied between 25% and 40%. XRD analysis showed that nominal and actual compositions were in agreement within 1-2% of Ge contents. The Si and SiGe layer stack deposition is repeated 20 times to form a SiGe/Si superlattice structure. In order to discuss the influence of the temperature after the SiGe growth on the SiGe nanodot formation, annealing at 725°C or 750°C is performed after each SiGe deposition step for selected samples.

X-ray diffraction (XRD) is used to characterize the vertical and lateral periodicity of SiGe dots and the crystal quality. Scanning electron microscopy (SEM) with energy-selective backscattered electron detector is used to check periodicity and surface morphology. Cross section transmission electron microscopy (TEM) and scanning TEM (STEM) are used to characterize SiGe dot geometry and crystal defects. Atomic force microscopy (AFM) is used for surface morphology analysis. Finally, a continuum growth model is exploited to better understand the main driving forces determining the observed body-centered ordering.

1 2 3 4 5 6 7 8 9 10 11 12 13 14 15 16 17 18 19 20 21 22 23 24 25 26 27 28 29 30 31 32 33 34 35 36 37 38 39 40 41 42 43 44 45 46 47 48 49 50 51 52 53 54 55 56 57 58 59 60

3. Vertical and lateral alignment of nanodot formation

Figures 1 a-c show cross section SEM images of SiGe/Si superlattice with a Ge content of 25%, 30% and 35%, respectively. SiGe and Si growth temperatures for all samples are 550°C and 700°C, respectively. We recall here that for Ge content of ~30%, the critical wetting layer thickness for island formation is predicted to quickly increase with decreasing Ge composition, and to be sensitive to variations in the deposition conditions [14]. This is confirmed by our findings. For instance, the sample with lower (25%) Ge content (Fig.1a) shows flat SiGe and Si layers. On the other hand, the SiGe/Si superlattices with slightly larger Ge contents, i.e. 30% and 35% (Fig. 1b and c), evidently exhibit SiGe nanodot formation. In both cases, the SiGe nanodots in one layer are formed between the SiGe nanodots of the adjacent layers, resulting in a staggered structure formation. A thin SiGe (wetting) layer is observed between SiGe nanodots in each layer. For both samples, the SiGe nanodot formation is weak and imperfect for the first layers and an ordered arrangement is only achieved after several cycles of SiGe/Si growth [15].

In Figure 2 we present AFM images of the SiGe/Si superlattice structure at different steps of growth: (a) after first SiGe layer deposition; (b) after post-annealing at 700°C (i.e. before first Si cap layer growth); (c) after first Si layer growth on the SiGe at 700°C; (d) after 20 cycles of SiGe layer deposition; (e) after 20 cycles of SiGe growth followed by postannealing at 700°C and (f) after final Si cap growth at 700°C. After the first SiGe layer deposition (Fig.

2a), a smooth surface (root mean square (RMS) roughness of 0.07 nm) is observed. SiGe nanodots are not visible. However, by introducing post-annealing at 700°C (Fig.2 b), the SiGe surface is roughened and nanodot formation occurs. We notice that this temperature is close to the critical condition for the formation of 3D clusters. The RMS roughness of the postannealed surface is 1.0 nm. As we observed for the first SiGe layer (Fig. 1b), the SiGe nanodot formation is imperfect and randomly distributed. By following Si cap deposition (Fig. 2c), the SiGe nanodots are embedded and become smoother (RMS roughness: 0.31 nm), but the surface roughness of the SiGe nanodots is transferred to the Si surface. On the other hand, after 20 cycles of SiGe/Si deposition (Fig. 2d), periodic SiGe nanodots are observed. The SiGe nanodots are well aligned along equivalent <010> directions, with the dot edges parallel to the <010> as well. The shallow SiGe nanodots feature a diameter and height of ~100 nm and ~1.7 nm, respectively. After annealing at 700°C (Fig. 2e), the surface roughens and the SiGe height is ~7.5 nm. Irregular structures of SiGe nanodots are observed at several places, as probably due to irregular strain distribution underneath. By depositing a Si cap at 700°C (Fig. 2f), square-shaped Si mesas having sidewalls parallel to the <110> directions and aligned along the <010> directions are observed in a checkerboard arrangement. The RMS surface roughness is 2.1 nm and the height of the Si squares is about 7.5 nm. The ordered Si mesas have the same in plane periodicity as the underlying SiGe nanodot.

An XRD reciprocal space mapping (RSM) of (004) diffraction in [110] plane of a 20

cycles periodic SiGe nanodot structure with 30% Ge content and 50 nm thick Si spacer is shown in Fig. 3. The periodicity of the diffraction peaks toward Qz direction is corresponding to the vertical distance of the SiGe planes. The distance of the diffraction peaks in Qz direction is 1.869×10^{-3}Å^{-1}, which results in average periodicity of SiGe of 53.5 nm. The distance of the diffraction peaks measured in Qx direction is 1.571×10^{-3}Å^{-1}, i.e. average periodicity in [110] direction is 96.4 nm. As shown in Fig. 2a and 2b, the lateral periodicity of SiGe nanodots in one plane is two times larger. The minimum distance of diffraction peaks in Qx direction corresponds to the lateral periodicity of these SiGe nanodots (189 nm) in one plane. The XRD RSM diffraction pattern indicates that most of the SiGe nanodots are regularly aligned.

4. Tuning the superlattice periodicity by variation of the deposition parameters

The process temperature dependence of the SiGe nanodot formation can be observed in Figures 4a-d, where we show cross section SEM images of SiGe/Si superlattice structures with 30% Ge content obtained with different annealing temperature before Si spacer growth. The growth temperature of Si in Fig. 4a is 675°C, and 700°C in Fig. 4b-d, respectively. After each SiGe growth step, an annealing is performed at 725°C and 750°C for samples shown in Fig. 4c and 4d, respectively. By capping with Si at 675°C, no SiGe nanodot formation is observed (Fig. 4a). In the case of Si growth at 700°C, SiGe nanodot formation occurs (Fig.

1
2
3
4
5
6
7
8
9
10
11
12
13
14
15
16
17
18
19
20
21
22
23
24
25
26
27
28
29
30
31
32
33
34
35
36
37
38
39
40
41
42
43
44
45
46
47
48
49
50
51
52
53
54
55
56
57
58
59
60

4b). The SiGe nanodots are located at staggered positions and form a BCT structure. By introducing an annealing step at 725°C after each SiGe layer deposition (Fig. 4c), a wider lateral periodicity of SiGe nanodots is observed compared to that of Fig. 4b. This means that it is possible to modulate the spacing of SiGe islands by changing the annealing temperature. By introducing an annealing at 750°C after each SiGe growth step (Fig. 4d), the arrangement of SiGe nanodots becomes irregular. Additionally, a diagonal SiGe nanodot alignment is observed at several places.

A cross-section STEM analysis was performed to better characterize the 3D island distribution. Images of SiGe nanodot structures with Si spacer deposited at 700°C without annealing, and with additional annealing at 725°C and 750°C after each SiGe growth steps are shown in Fig. 5a-c, respectively. The top layer of all samples is as-deposited SiGe (process is finished at 550°C). In the case of the sample without annealing (Fig. 5a), SiGe nanodots are regularly aligned at staggered positions as shown in Fig. 4b. SiGe nanodots mean diameter and height are ~110 nm and ~20 nm, respectively. The periodicity of SiGe nanodots is about 200 nm. SiGe layers 2-3 nm thick are clearly visible between the SiGe nanodots. The thickness of the top SiGe layer is larger where the underlying Si layer is concave. This is in agreement to what we reported, supporting the roughness reduction of the surface by covering with SiGe (shown in Fig. 2d compared to 2f), and the SiGe surface migration during temperature ramp from 550°C to 700°C (Fig. 2e). The Si thickness on the SiGe nanodots and

in the concave part between SiGe nanodots is nearly the same, resulting in almost the same surface roughness before and after Si growth, and following the periodicity transfer from SiGe nanodots to the Si surface. The Si surface above each SiGe nanodot shows a flat (100) surface. On the other hand, the Si surface grown on the thin SiGe layer between nanodots exhibits a concave shape. By introducing an additional annealing at 725°C after each SiGe deposition (Fig. 5b), the SiGe nanodot staggered alignment is preserved and the Si thickness between SiGe nanodot layers remains uniform while the diameter of the SiGe nanodot increases to 135 nm and the lateral periodicity is increased to ~260 nm. The height of the SiGe nanodots is about 20 nm, which is nearly the same as in Fig. 5a. Enhanced SiGe migration seems to occur by introducing an annealing at 725°C. After annealing at 750°C (Fig. 5c), the SiGe nanodots become larger and an irregular alignment is observed as already shown in Fig. 4d. Even though the SiGe nanodot formation becomes irregular, no crystal defects could be observed (confirmed by both STEM and TEM analysis). This means that the irregularity of SiGe nanodot formation is not triggered by crystal defects. It seems that Si growth on large SiGe nanodots is not uniform, because thinner Si regions are observed at several positions. By the non-uniform Si growth, the periodicity of SiGe nanodots seems to be not perfectly transferred to the Si surface. However, further investigations are required to clarify the mechanism behind.

In Fig. 6, the lateral periodicity of SiGe nanodots is plotted as a function of annealing

1 2 3 4 5 6 7 8 9 10 11 12 13 14 15 16 17 18 19 20 21 22 23 24 25 26 27 28 29 30 31 32 33 34 35 36 37 38 39 40 41 42 43 44 45 46 47 48 49 50 51 52 53 54 55 56 57 58 59 60

temperature before Si spacer growth. The Si growth temperatures for the sample with annealing at 675°C and the other samples are 675°C and 700°C, respectively. That means an additional annealing is performed for the samples with 725°C and 750°C annealing. In the case of sample with 30% Ge content, no SiGe nanodot formation occurred at 675°C as shown in Fig. 4a. However, a periodic SiGe nanodot formation appears in the case of samples with 35% Ge content. The possible reason for periodic nanodot formation for 35% SiGe samples is the higher driving force of SiGe migration due to higher strain. As shown in Fig. 4b-d, the lateral periodicity of SiGe nanodots becomes higher with increasing annealing temperature. At the same annealing temperature, samples with 35% Ge content show slightly higher periodicity compared to those with 30% Ge content.

The lateral periodicity of SiGe nanodots as a function of Si spacer thickness and SiGe thickness are shown in Fig. 7a and b, respectively. Temperatures of SiGe and Si growth are 550°C and 700°C, respectively for all cases. With increasing Si spacer thickness (Fig. 7a), the periodicity of the SiGe nanodot increases and tends to saturate. The influence of Ge concentration on the periodicity is weak for each Si spacer thicknesses. On the other hand, the lateral periodicity weakly increases with increasing SiGe thickness (Fig. 7b). The periodic SiGe nanodots are formed by Si and Ge atom migration into the concave areas of the Si surface to reduce surface energy. The SiGe nanodots are formed after accumulation into the concave region in order to provide strain relaxation. This effect can be related to the

expansion of the distance between the SiGe layer and the underlying Si spacer.

5. Continuum growth simulations and interpretation of the observed stacking

We shall now provide an interpretation for the above reported BCT stacking of SiGe nanodots. As shown in Fig. 2f, once dots are formed, Si deposition does not lead to a flat capping layer: The free surface presents bumps in correspondence to buried islands and valleys in between. Thus, when the subsequent SiGe layer is deposited, the morphology of the substrate resembles that of a pit-patterned Si substrate, leading to preferential island positioning within the pits [16-18]. However, such driving force towards staggered vertical arrangement, mainly generated by surface-energy reduction, competes with the epitaxial strain reduction, known to favor vertical alignment instead [19, 20].

In order to better understand the competition between these two mechanisms leading to different vertical ordering, we have used a 2D continuum model of heteroepitaxial growth, implemented in a phase-field framework as detailed in Ref. [21]. The growth dynamics is determined both by material deposition and by surface diffusion. A thermodynamic driving force, based on the minimization of the free energy, is assumed for material redistribution on the surface, so that material flow (J) on the surface is driven by the local gradient of the chemical potential (μ): $J=-D\nabla\mu$. The evolution of the surface profile, expressed by the normal velocity (v), can be written as $v=-\nabla\bullet J$ by imposing the volume conservation as in a pure

diffusion-limited growth regime, where D is the diffusion coefficient. The chemical potential results as the balance of two different contributions, one from surface energy and the other from the elastic energy. While the former is proportional to the profile curvature and favors a flattening of the surface, the latter accounts for the exact solution of elastic strain field at the surface, obtained by imposing a mechanical equilibrium condition, which is originated by the misfit strain between SiGe layers and Si substrate (~ -1.3%) and leads to the growth of islands. Material deposition is simulated as a constant isotropic flux impinging on the surface along its normal. Here we impose a sufficiently large ratio (2.5×10^5) between the diffusion coefficient D and the deposition flux, so to ensure that material diffuses towards the local minimum of the chemical potential.

In the model, the surface energy density γ and the Lamé coefficients are linearly interpolated for a 30% Ge content, starting from the typical values found in literature for Ge and Si (γ_{Ge}=6 eV/nm^2, γ_{Si}=9 eV/nm^2, μ_{Ge}=41 GPa, λ_{Ge}=44 GPa, μ_{Si}=52 GPa, λ_{Si}= 60GPa [23]). The set of partial differential equations, which defines both the film evolution and the mechanical equilibrium problem, is exactly solved by a finite element method, exploiting the AMDiS toolbox [22, 24] (see Ref. [23] for the numerical implementation). This provides us both a nonlinear description for the surface diffusion process and an exact solution for the strain field. Therefore, the model is able to precisely capture the effect of the buried islands on the strain at the surface and the role of surface roughness of the Si capping layer.

1 2 3 4 5 6 7 8 9 10 11 12 13 14 15 16 17 18 19 20 21 22 23 24 25 26 27 28 29 30 31 32 33 34 35 36 37 38 39 40 41 42 43 44 45 46 47 48 49 50 51 52 53 54 55 56 57 58 59 60

To show the influence of the surface roughness on the ordering process, at first we considered a layer of islands with cosine-like distribution whose average roughness (1 nm), periodicity (150 nm), and Ge composition (30%) were directly inferred from the experiments. Importantly, the average roughness (0.43 nm) of the Si spacing layer (25 nm thick) was also set based on experiments, with the surface profile maxima being superimposed to buried island (Fig. 8a) . To save on simulation time, we have focused solely on the alignment of a single layer of SiGe islands on top of a layer of islands capped with Si, rather than considering the whole island stack which we assume follows the same evolution of the first "module".

In the initial stages, the SiGe material deposited on the Si cap layer flows toward the surface valleys for a capillarity effects, lowering the surface energy by decreasing the free surface. In these valleys, the elastic relaxation is enhanced because the strain can be partially transferred to the valley sidewalls, similarly to what typically happens in the growth of islands on pit-patterned substrates [23]. Therefore, the chemical potential on the surface becomes lower in these regions, thanks to this additional elastic relaxation. Consequently, the material is accumulated there leading to the island staggered arrangement with respect to the buried ones. It is worth noticing that the staggered alignment is observed despite the initial strain relaxation distribution at the surface, induced by the buried islands, would favor a vertically aligned growth [25, 26].

To directly assess the role played by the initial roughness of the Si capping layer, we have repeated the simulations by artificially decreasing it by one order of magnitude (Fig. 8b). The surface-energy reduction due to the filling of the surface valleys is weaker than before. Therefore, the elastic relaxation provided by the buried islands is the predominant driving force of the diffusion dynamics, as can be observed by the deposited material accumulation on top of the buried islands, leading to a vertical stacking.

It is worth to notice that the vertically aligned islands exhibit a slightly lower compressive strain than the anti-aligned ones, i.e., in the former case, the elastic energy in the islands is lower thanks to the additional relaxation provided by the buried islands. This also indicates that it is fundamental to follow the full growth pathway to determine the final alignment.

The important role played by surface roughness in promoting vertical anti-alignment was recently discussed in Ref. [27], where ordering of Ge quantum dots in an amorphous matrix is investigated by Kinetic Monte Carlo simulations. Notice that in the present case of a crystalline matrix the situation is more complex, as surface-roughness promoted ordering competes with strain relaxation.

We also point out that Liu et al. [28] reported, based on a continuum approach similar to the present one, the existence of a growth-parameter window where vertical anti-alignment could take place also in the absence of surface roughness. A similar conclusion was also

1 2 3 4 5 6 7 8 9 10 11 12 13 14 15 16 17 18 19 20 21 22 23 24 25 26 27 28 29 30 31 32 33 34 35 36 37 38 39 40 41 42 43 44 45 46 47 48 49 50 51 52 53 54 55 56 57 58 59 60

drawn by Latini et al. for III/V systems [29]. While not ruling out the importance of such results under different conditions, here we have shown that for the present system and growth parameters roughness plays, instead, a decisive role.

6. Summary and Conclusions

Self-ordered multi SiGe nanodot layer stacks are fabricated by depositing SiGe/Si superlattice layer stacks using an RPCVD system. In the case of SiGe/Si superlattice with 30% Ge content, a 3D lattice of periodic SiGe nanodots is formed, if the Si growth is 700°C or above. The SiGe nanodots are aligned at staggered positions by annealing at 700°C and 725°C before each Si spacer growth, resulting in a BCT SiGe nanodot structure. No SiGe nanodots are formed in the case of 25% Ge content or by lowering the Si spacer growth temperature from 700°C to 675°C, indicating that the SiGe nanodot formation is caused by elastic strain compensation due to surface migration. The lateral periodicity can be modulated by the annealing temperature before the Si growth and the thickness of SiGe. Only a weak influence of the Ge concentration on the periodicity is observed. The peculiar island distribution was interpreted on the base of continuum growth simulations, pointing out the competition between the vertical alignment induced by the strain field of the buried nanodots and the vertical anti-alignment produced by the surface roughness of the capping layer. The latter term is of key importance for the present group-IV system as anisotropy-related driving forces

1
2
3
4
5
6
7
8
9
10
11
12
13
14
15
16
17
18
19
20
21
22
23
24
25
26
27
28
29
30
31
32
33
34
35
36
37
38
39
40
41
42
43
44
45
46
47
48
49
50
51
52
53
54
55
56
57
58
59
60

leading to complex stacking in other systems (such as II/VI or III/V semiconductors) are expected to be negligible.

1 2 3 4 5 6 7 8 9 10 11 12 13 14 15 16 17 18 19 20 21 22 23 24 25 26 27 28 29 30 31 32 33 34 35 36 37 38 39 40 41 42 43 44 45 46 47 48 49 50 51 52 53 54 55 56 57 58 59 60

References

[1] J.M. Hartmann, P. Holliger, F. Laugier, G. Rolland, A. Suhm, T. Ernst, T. Billon and N. Vulliet, J. Cryst. Growth, 283 1-2 (2005) 57-67.

[2] O Leifeld, R Hartmann, E Müller, E Kaxiras, K Kern and D Grützmacher, Nanotechnology 10 (1999) 122–126.

[3] K.L. Wang, S. Tong and H.J. Kim, Mat. Sci. in Semicond. Proc. 8 (2005) 389 - 399

[4] K. Makihara, M. Ikeda, S. Higashi and S. Miyazaki, Thin Solid Films, 517, (1), (2008) 306-308.

[5] C. J.R.P. Augusto and Lynn Forester, Solid-State Electron. 110 (2015) 1-9

[6] K.L.Wang, D. Cha, J. Liu, C. Chen, Ge/Si self-assembled quantumdots and their optoelectronic device applications, Proc. IEEE 95 (2007) 1866–1883

[7] M. Grydlik, F. Hackl, H. Groiss, M. Glaser, A. Halilovic, T. Fromherz, W. Jantsch, F.Schäffler, M. Brehm, Lasing from glassy Ge quantum dots in crystalline Si, ACS Photonics 3 (2016) 298–303

[8] K. Brunner, Rep. Prog. Phys. 65, 27 (2002)

[9] D. Grützmacher, T. Fromherz, Ch. Dais, J. Stangl, E. Müller, Y. Ekinci, H. H. Solak, H. Sigg, R. T. Lechner, E. Wintersberger, St. Birner, V. Holý, and G. Bauer, Nano Letters **7**, 3150 (2007).

[10] Z.Y. Zhong and G. Bauer, Appl. Phys. Lett. 84, 1922 (2004).

1
2
3
4
5
6
7
8
9
10
11
12
13
14
15
16
17
18
19
20
21
22
23
24
25
26
27
28
29
30
31
32
33
34
35
36
37
38
39
40
41
42
43
44
45
46
47
48
49
50
51
52
53
54
55
56
57
58
59
60

[11] G. Capellini, M. De Seta, F. Evangelisti, and C. Spinella, Applied Physics Letters 82, 1772 (2003)

[12] J. Tersoff, C. Teichert, and M.G. Lagally, Phys. Rev. Lett. 76, 1675 (1996)

[13] F. Montalenti, A. Margegalli, G. Capellini, M. De. Seta and L. Miglio, J. Phys.: Condens. Matter 19 225001 (2007)

[14] Y. Tu and J. Tersoff, Phys. Rev. Lett. 93, 216101 (2004)

[15] J. Tersoff, C. Teichert, and M.G. Lagally, Phys. Rev. Lett. 76, 1675 (2006)

[16] Z.Y. Zhong and G. Bauer, Appl. Phys. Lett. 84, 1922 (2004)

[17] R. Bergamaschini, F. Montalenti, and L. Miglio, Nanoscale Res. Lett. 5, 1873 (2010)

[18] R. Bergamaschini, J. Tersoff, Y. Tu, J.J. Zhang, G. Bauer, and F. Montalenti, Phys. Rev. Lett. 109, 156101 (2012)

[19] J. Tersoff, C. Teichert, and M.G. Lagally, Phys. Rev. Lett. 76, 1675 (2006)

[20] G. Capellini, M. De Seta, F. Evangelisti, and C. Spinella, Applied Physics Letters 82, 1772 (2003)

[21] R. Bergamaschini, M. Salvalaglio, R. Backofen, A. Voigt and F. Montalenti, *Adv. in Phys.: X* **1**, 331 (2016)

[22] S. Vey and A. Voigt, Comput. Visualization Sci. **10**, (2007) 57

[23] M. Albani, R. Bergamaschini anf F. Montalenti, Phys. Rev. B **94** 075303 (2016).

[24] T. Witkowski, S. Ling, S. Praetorius and A. Viogt, Adv. Comput. Math. **41** 1145 (2015)

1
2
3
4
5
6
7
8
9
10
11
12
13
14
15
16
17
18
19
20
21
22
23
24
25
26
27
28
29
30
31
32
33
34
35
36
37
38
39
40
41
42
43
44
45
46
47
48
49
50
51
52
53
54
55
56
57
58
59
60

[25] J. Tersoff, C. Teichert, and M. G. Lagally, Phys. Rev. Lett. 76, 1675 (1996)

[26] G. Capellini, M. De Seta, F. Evangelisti, and C. Spinella, Applied Physics Letters 82, 1772 (2003).

[27] J. Endres, V. Holy, S. Danis, and M. Buhan, J. Nanopart. Res. 19, 135 (2017)

[28] P. Liu, Y.W. Zhang, and C. Lu, Phys. Rev. B 68, 195314 (2003)

[29] V. Latini, E. Placidi, F. Arciprete, E. Tisbi, F. Patella, and R. Magri, J. Appl. Phys. 120, 125704 (2016)

1
2
3
4
5
6
7
8
9
10
11
12
13
14
15
16
17
18
19
20
21
22
23
24
25
26
27
28
29
30
31
32
33
34
35
36
37
38
39
40
41
42
43
44
45
46
47
48
49
50
51
52
53
54
55
56
57
58
59
60

Figure captions

Figure 1. Cross section SEM images of 20 cycles of SiGe/Si superlattice structures. Ge concentrations are (a) 25%, (b) 30% and (c) 35%. Target SiGe and Si spacer thickness are 5 nm and 25 nm, respectively. SiGe and Si growth temperature are 550°C and 700°C, respectively.

Figure 2. AFM images of surface morphology of single layer of (a) as deposited 5 nm thick SiGe (b) 5 nm thick SiGe after postannealing at 700°C, (c) 50 nm thick Si on 5 nm thick SiGe, (d) SiGe/Si superlattice structures (20 cycles) with 30% Ge content, (e) and SiGe/Si superlattice (20 cycles) after postannealing at 700°C and (f) SiGe/Si superlattice (20 cycles) with additional 50 nm thick Si cap. Ge content in SiGe layers are 30%. Growth temperature of SiGe and Si are 550°C and 700°C, respectively. Top surface of (a, b, d, e) are SiGe and (c, f) are Si.

Figure 3. XRD-RSM of (004) diffraction in [110] plane measured on a 20 cycles of periodic SiGe nanodot structure with 50 nm thick Si spacer. Target SiGe thickness and Ge concentration are 5 nm and 30%, respectively. Vertical and horizontal periodicities calculated from diffraction peaks in the reciprocal space are shown in figure.

1 2 3 4 5 6 7 8 9 10 11 12 13 14 15 16 17 18 19 20 21 22 23 24 25 26 27 28 29 30 31 32 33 34 35 36 37 38 39 40 41 42 43 44 45 46 47 48 49 50 51 52 53 54 55 56 57 58 59 60

Figure 4. Cross section SEM images of SiGe/Si superlattice structures (20 cycles) with 30% Ge content. Target SiGe and Si spacer thickness are 5 nm and 50 nm, respectively. SiGe growth temperature for all samples is 550°C. Si growth temperature of a) is 675°C and 700°C for b-d). For c) and d), additional annealing is performed after each SiGe growth at 725°C and 750°C, respectively. Positions of diagonal alignment of SiGe nanodots are indicated by arrows.

Figure 5. Cross section STEM images of SiGe/Si superlattice structures (20 cycles) with 30% Ge content. SiGe and Si growth temperatures are 550°C and 700°C, respectively. For b) and c), additional annealing is performed after each SiGe growth at 725°C and 750°C, respectively.

Figure 6. Lateral periodicity as a function of annealing temperature before Si growth. SiGe growth temperature is 550°C for all samples. Growth temperatures for the sample with 675°C annealing and other samples are 675°C and 700°C, respectively. Target SiGe thickness and Si thickness are 5 nm and 50nm, respectively. The Si growth temperatures are indicated for all samples.

Figure 7. Lateral periodicity as a function of (a) Si spacer and (b) SiGe thickness. SiGe and

Si growth temperatures are 550°C and 700°C, respectively. The SiGe thickness of (a) is 5 nm and the Si thickness of (b) is 25 nm. Ge concentration in SiGe is varied from 30% to 40%.

Figure 8. Phase-field simulations of island stacking. Growth of SiGe nanodots with 30% Ge content on a 25 nm thick Si cap layer, which is covering the first layer of buried SiGe nanodots. Three stages are shown for different amounts of deposited material (h_d). In Fig. 8a, the surface RMS roughness of the Si capping layer is set to 0.43 nm. In the intermediate stage, the strain in the film is lower in the valley regions. This leads to an anti-aligned ordering of islands. In Fig. 8b, the surface roughness of the Si capping is reduced by ten times. In the intermediate stage, the strain in the film is lower upon the buried islands. This finally leads to a vertically aligned stacking. The color map represents the in-plane strain component (ε_{xx})

1
2
3
4
5
6
7
8
9
10
11
12
13
14
15
16
17
18
19
20
21
22
23
24
25
26
27
28
29
30
31
32
33
34
35
36
37
38
39
40
41
42
43
44
45
46
47

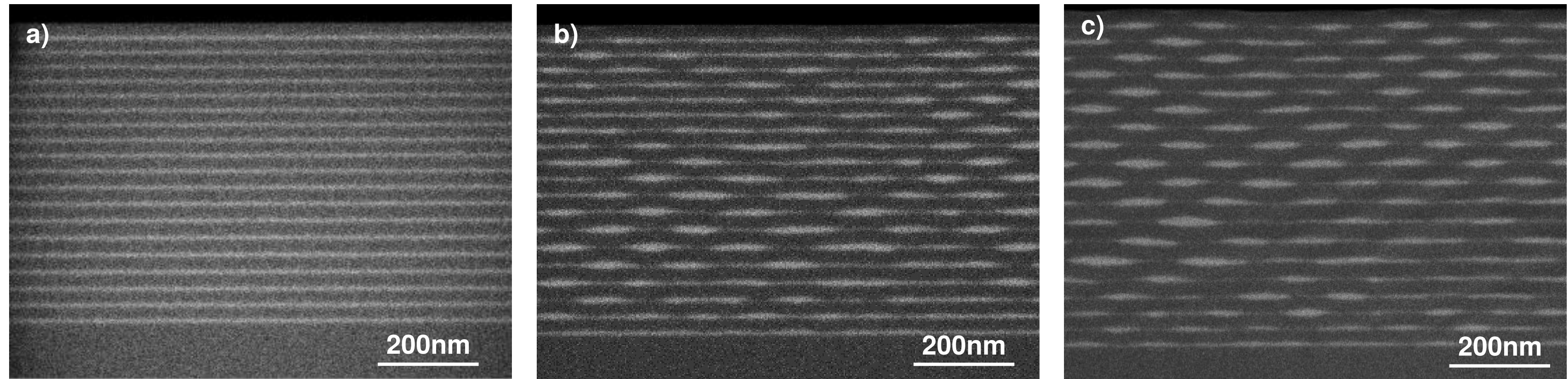

Fig. 1. Y. Yamamoto et al.

1
2
3
4
5
6
7
8
9
10
11
12
13
14
15
16
17
18
19
20
21
22
23
24
25
26
27
28
29
30
31
32
33
34
35
36
37
38
39
40
41
42
43
44
45
46
47

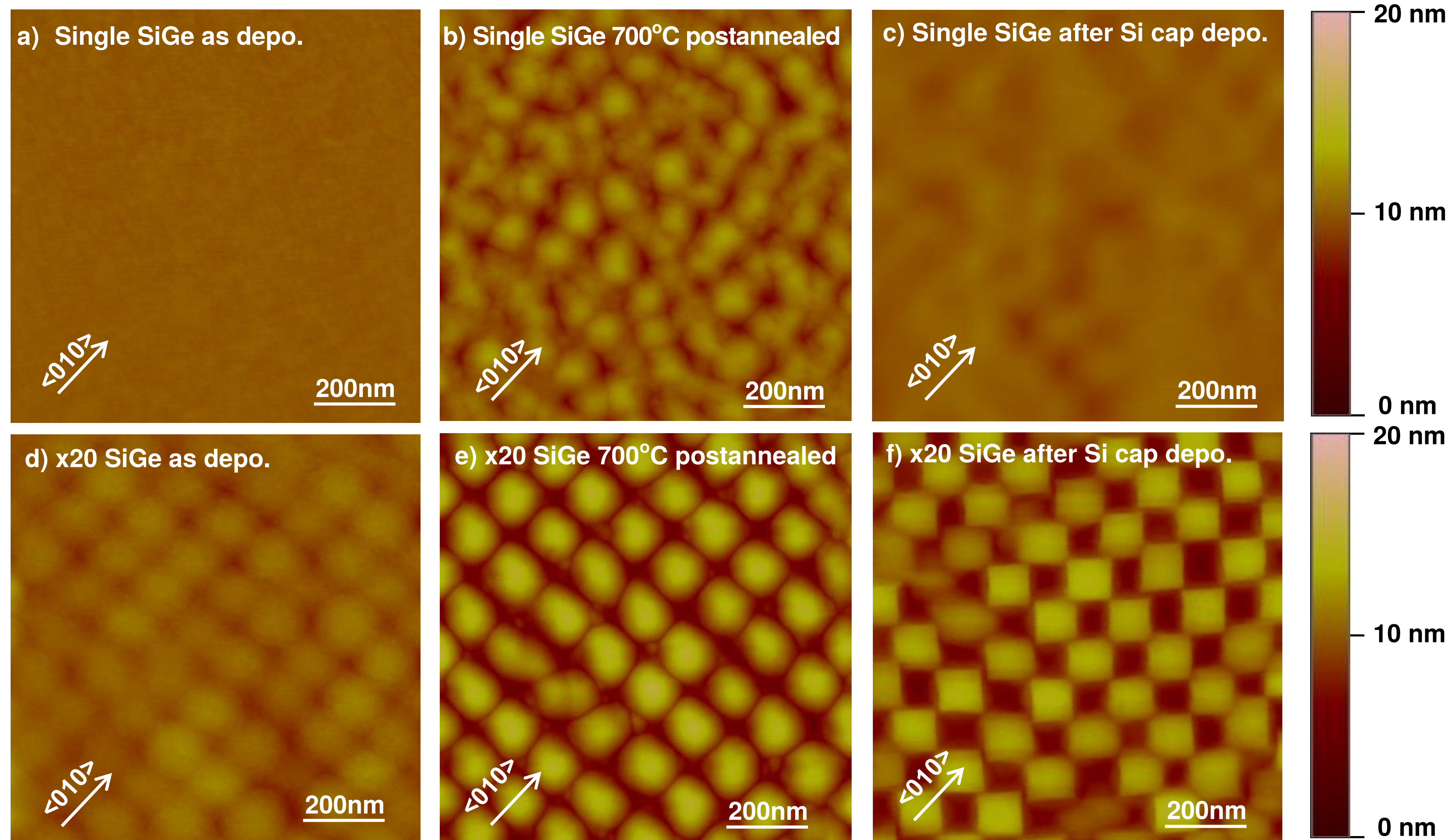

Fig. 2. Y. Yamamoto et al.

1
2
3
4
5
6
7
8
9
10
11
12
13
14
15
16
17
18
19
20
21
22
23
24
25
26
27
28
29
30
31
32
33
34
35
36
37
38
39
40
41
42
43
44
45
46
47

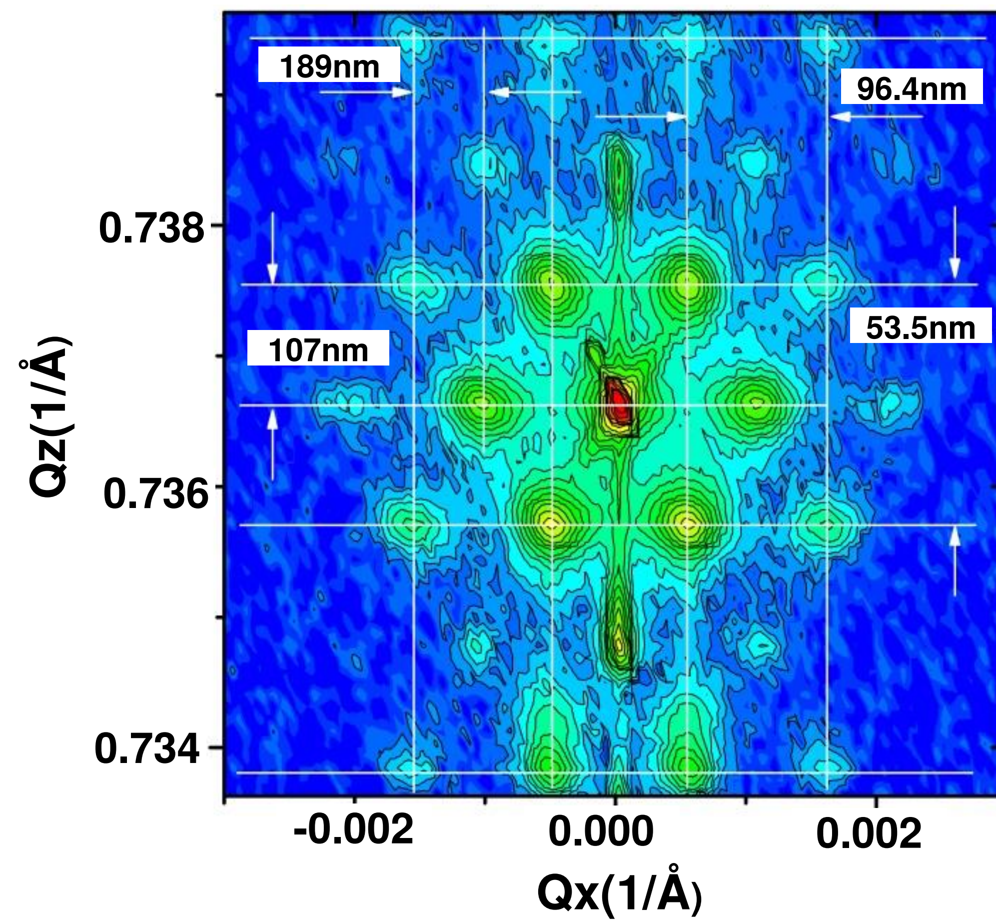

Fig. 3. Y. Yamamoto et al.

1
2
3
4
5
6
7
8
9
10
11
12
13
14
15
16
17
18
19
20
21
22
23
24
25
26
27
28
29
30
31
32
33
34
35
36
37
38
39
40
41
42
43
44
45
46
47

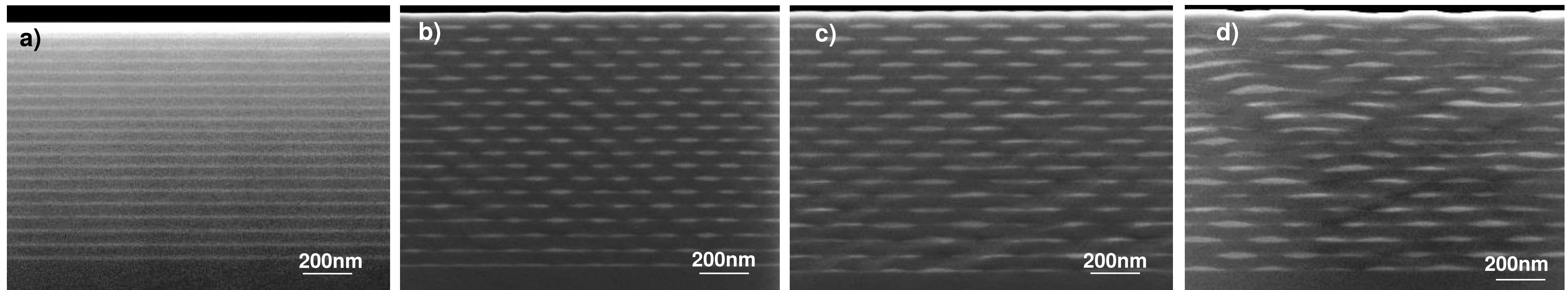

Fig. 4. Y. Yamamoto et al.

1
2
3
4
5
6
7
8
9
10
11
12
13
14
15
16
17
18
19
20
21
22
23
24
25
26
27
28
29
30
31
32
33
34
35
36
37
38
39
40
41
42
43
44
45
46
47

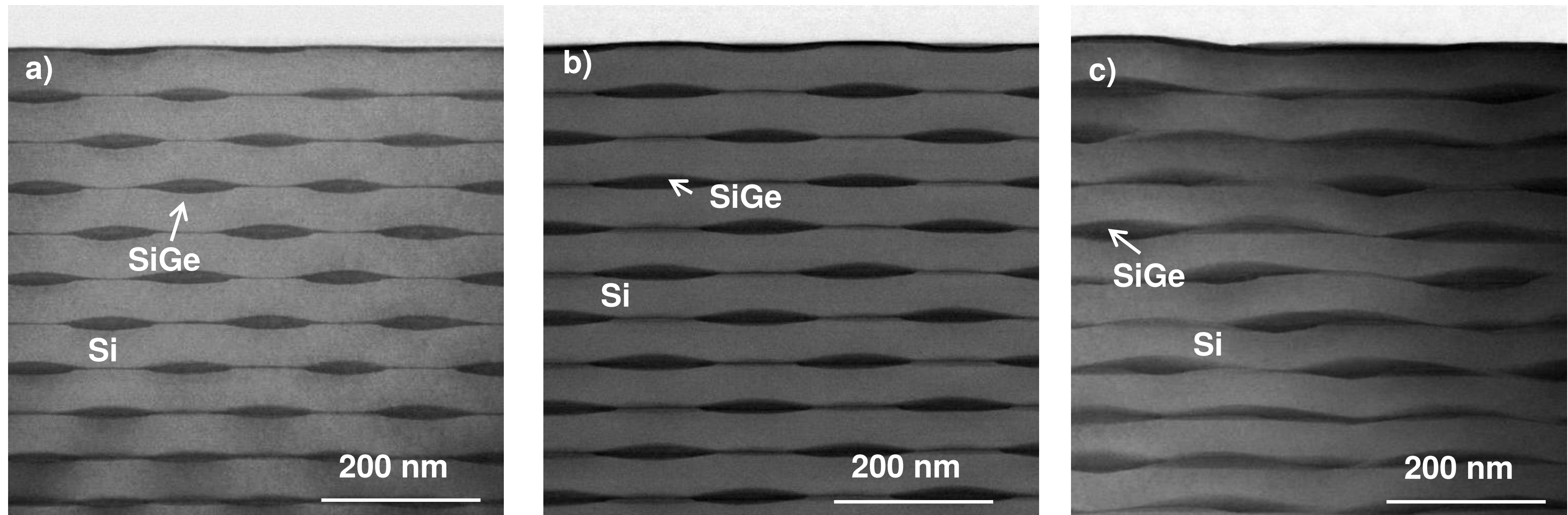

Fig. 5. Y. Yamamoto et al.

1
2
3
4
5
6
7
8
9
10
11
12
13
14
15
16
17
18
19
20
21
22
23
24
25
26
27
28
29
30
31
32
33
34
35
36
37
38
39
40
41
42
43
44
45
46
47

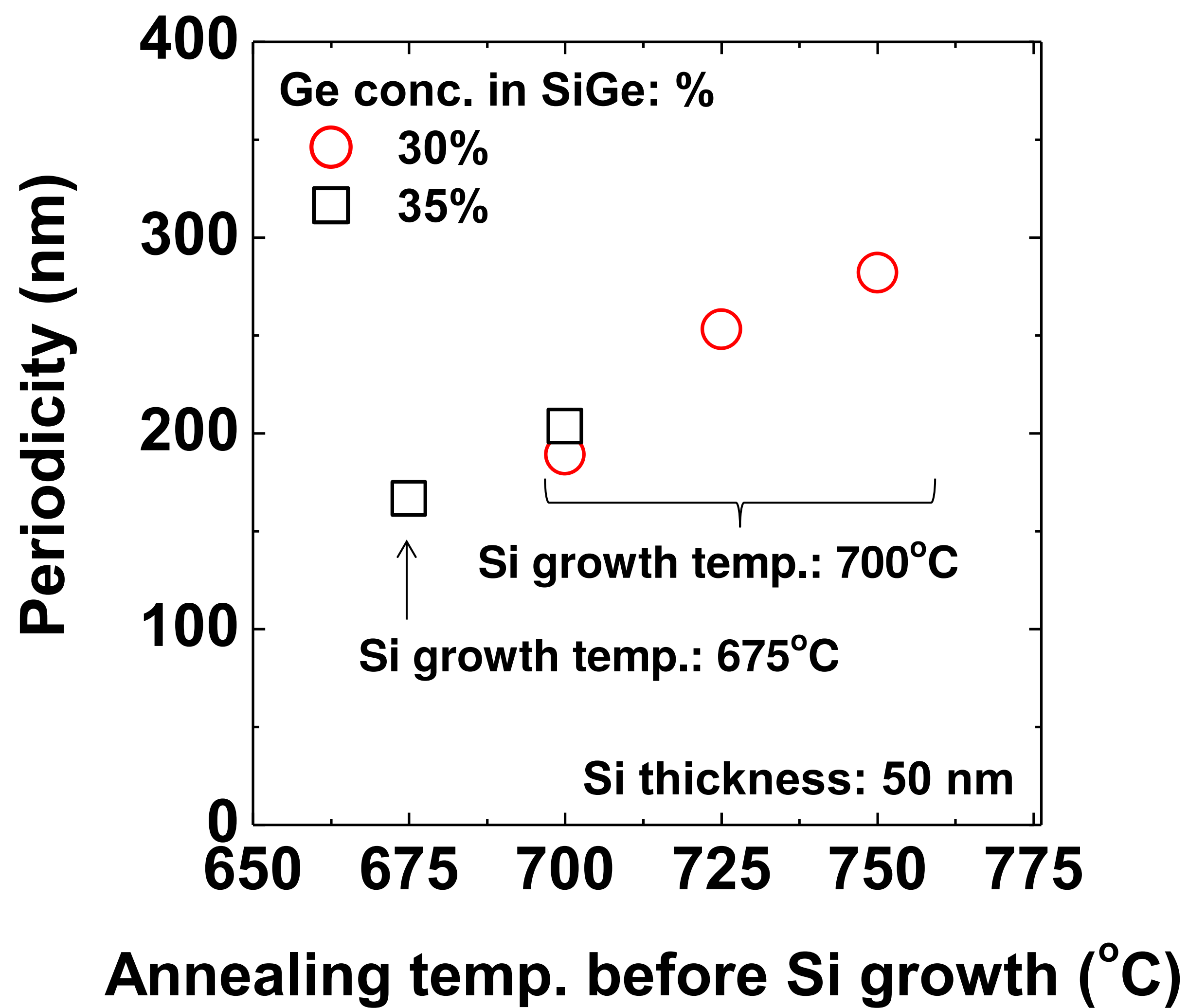

Fig. 6. Y. Yamamoto et al.

1
2
3
4
5
6
7
8
9
10
11
12
13
14
15
16
17
18
19
20
21
22
23
24
25
26
27
28
29
30
31
32
33
34
35
36
37
38
39
40
41
42
43
44
45
46
47

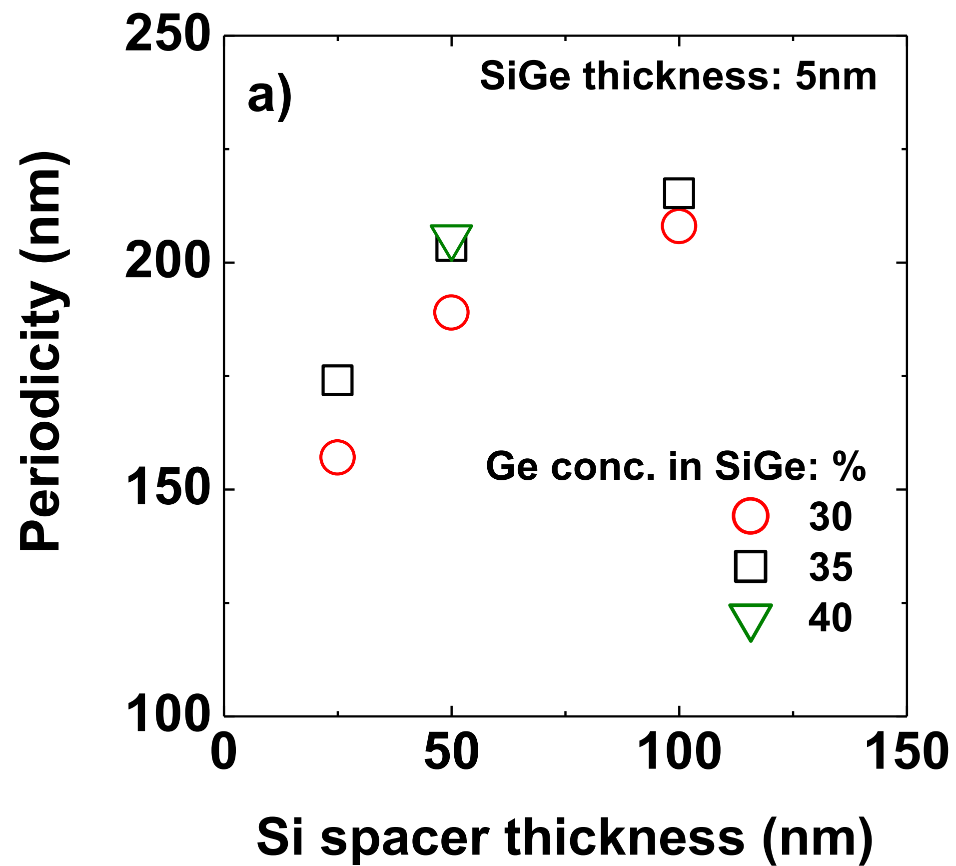

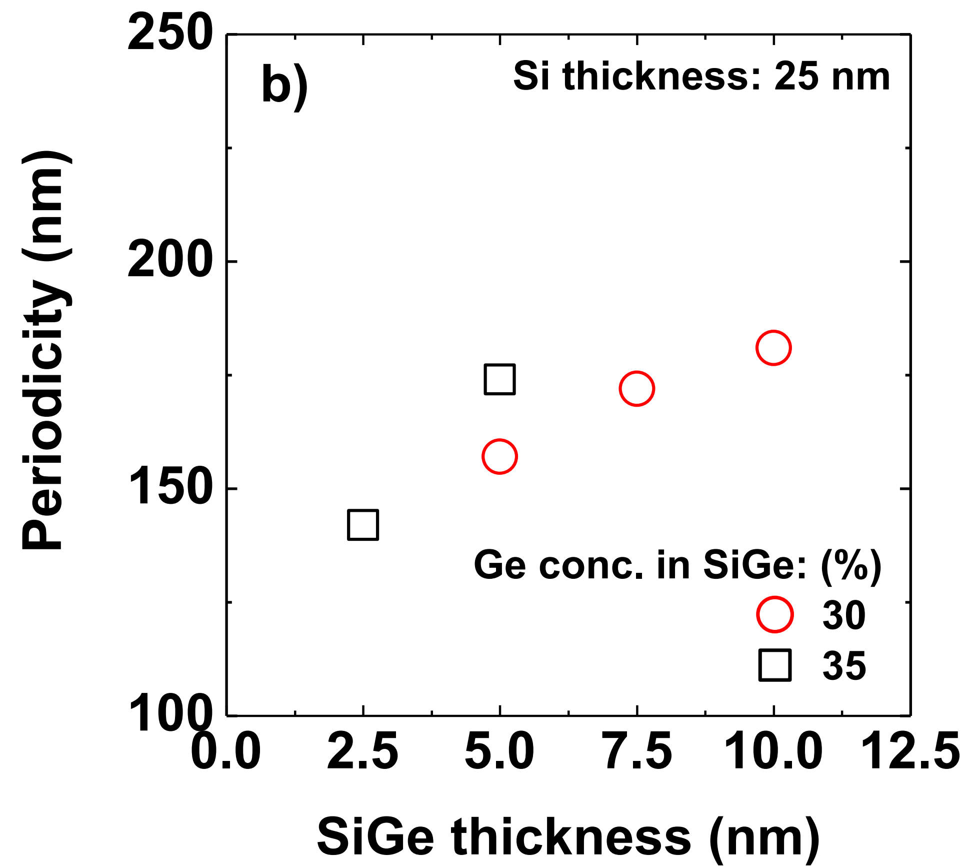

Fig. 7. Y. Yamamoto et al.

1
2
3
4
5
6
7
8
9
10
11
12
13
14
15
16
17
18
19
20
21
22
23
24
25
26
27
28
29
30
31
32
33
34
35
36
37
38
39
40
41
42
43
44
45
46
47

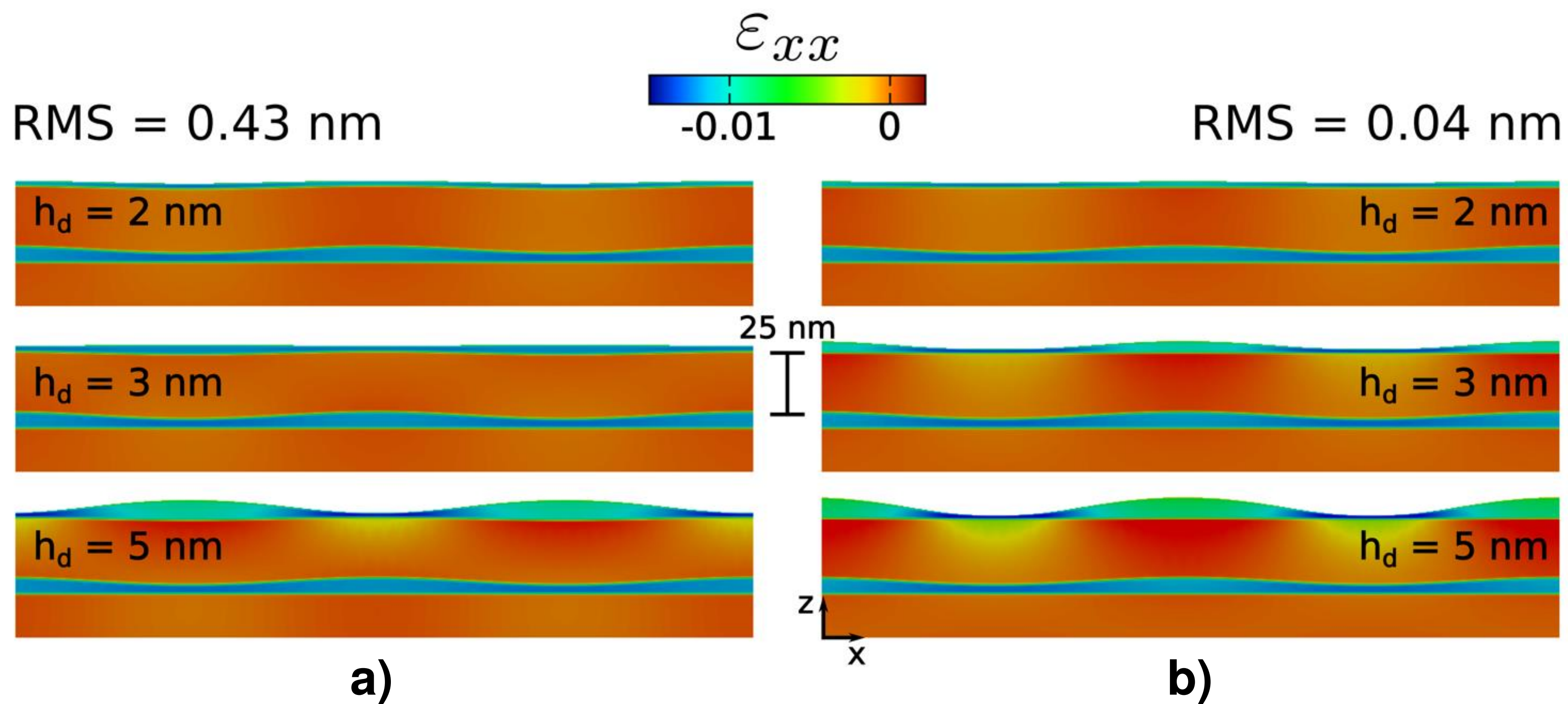

Fig. 8. Y. Yamamoto et al.